Supporting Materials

Electronic-mechanical coupling in graphene from in-situ nanoindentation experiments and multiscale atomistic simulations

Mingyuan Huang[†,*], Tod A. Pascal[§,‡], Hyungjun Kim[§,‡], William A. Goddard III[§,‡], Julia R. Greer[†]

[†]Division of Engineering and Applied Science, California Institute of Technology, 1200 E. California Blvd, MC 309-81, Pasadena, California 91125-8100, USA.
[§]Center for Materials Simulations and Design, Graduate School of EEWS, Korea Advanced Institute of Science and Technology, Daejeon, Korea
[‡]Materials and Process Simulation Center, California Institute of Technology, 1200 E. California Blvd, MC 309-81, Pasadena, California 91125-8100, USA.
[*]To whom correspondence should be addressed. E-mail: mingyuan@caltech.edu. Tel: 626-395-2243.

Sample fabrication:

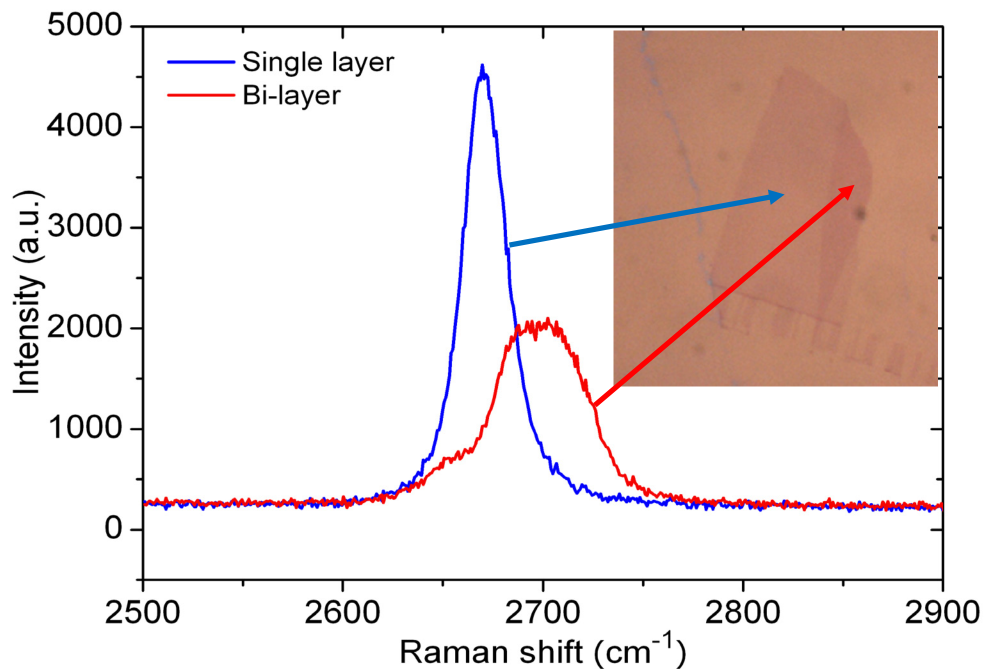

Figure S1, Raman spectra of the 2D mode of single layer and bi-layer graphene. The Raman spectrum (blue curve) was taken from the thinner area part of the graphene flake (an optical image was shown in the inset). The sharp symmetric peak at about 2680 cm^{-1} proves that the thinner part of the flake is single layer graphene. The broad and asymmetric nature of the Raman spectrum (red curve) taken from the thicker part of the flake shows that the thicker part is bi-layer graphene.

The first step in our fabrication process is mechanical exfoliation of the graphene flakes onto SiO_2/Si wafer by the well-known 'Scotch tape' method[1]. Single layer graphene flakes are identified based on their optical contrast and confirmed by Raman spectroscopy[2], shown in Fig. S1. To ensure that strain is uniform during the nanoindentation experiment, graphene flakes were shaped into graphene ribbons with the widths between 1.5 to 4 μm by E-beam lithography and subsequent argon plasma etching. The electrodes were patterned by E-beam lithography with the separation from 0.8 to 1.2 μm. Thin films comprising the electrodes, 3 nm-thick Cr under 100~200 nm-thick Au, were deposited by e-beam evaporation, followed by acetone "lift-off" process. The large thickness of the

electrodes was chosen to increase their stiffness. Finally, Buffered Oxide Etchant (BOE, 50:1) was used to etch the underlying SiO_2 and critical point dryer was used to release the suspended graphene (Fig. 1b). Because BOE can diffuse freely under the graphene ribbons[3], the SiO_2 under graphene ribbons, including the part under the electrodes, was etched away at the same rate and left a constant distance (~200 nm) between the graphene ribbons and the substrate. Thus, the part of the electrodes with the graphene is also suspended, as shown in Fig. 1c.

The 8 μm-wide wedge tip with ~15° angle was fabricated from a standard Berkovich indenter tip by focused ion beam (FIB) and coated with 30 nm Al_2O_3 by a magnetron sputtering system to electrically isolate the graphene from the indenter tip. The nanoindentation tests were performed at a constant displacement rate of 2 nm/s controlled by a custom-written feedback-loop algorithm. As shown in Fig. 1b, the graphene devices were made in two-terminal configuration to ensure uniform strain during the nanoindentation experiment, and the highly doped Si substrate was taken as the gate. Graphene devices were mounted in the standard chip carriers (the up-right inset in Fig. 2a) and the electrical measurements were carried out by a Keithley source meter. To incorporate the electrical measurements into the nanoindentation tests, several intentional load holds were added during loading and the electrical tests were performed during these holds.

Stiffness of gold electrodes:

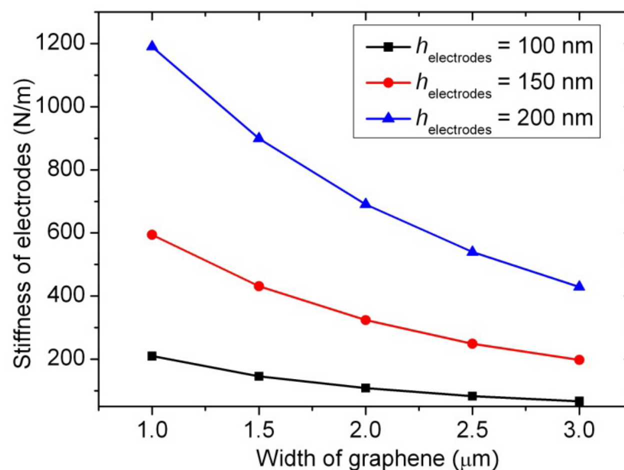

Figure S2. The simulated stiffness of the electrodes was plotted as a function of width of graphene for three different thicknesses of electrodes.

As we can observe in the nanoindentation video, the supporting electrodes aren't infinitely stiff and they bend when graphene is stretched. To figure out how much the electrodes deflected, the stiffness of the electrodes was simulated by using finite element method (ABAQUS). As shown in Fig. 1c, the part of electrodes with graphene underneath was suspended due to the BOE freely diffusing along the graphene ribbon. Also, 200 nm undercut was taken into account for all edges. Because the bending is mainly perpendicular to the electrodes and no slippage between the electrodes and graphene occurs, only the perpendicular stretching force was considered and the average

displacement of the interface between the graphene and the electrodes was taken as the displacement of the electrodes. The stiffness of the electrodes was then extracted out and plotted in Figure S2 as a function of width of graphene and thickness of electrodes. The deflection of the electrodes as calculated based on this stiffness, was then taken out from the total displacement of the indenter tip.

Gate capacitance

The back gate capacitance of suspended device can be estimated as:

$$C_{back}/A_{graphene} = \frac{\epsilon_0 \epsilon_r}{d_0 + \epsilon_r d_1} = 3.9 \ \text{(nF/cm}^{-2}\text{)} \tag{S1}$$

As we described before, the standard B-doped diamond Berkovich indenter tip (the width of the tip is about 100 nm) was shaped by the focus ion beam into a wedge-shaped tip. A layer of 30 nm thick Al_2O_3 was then coated on the tip surface to create an insulating layer between the grahene and the indenter head. When the indenter tip touches the graphene device, the capacitance between the graphene and the indenter tip can be calculated:

$$C_{tip}/A_{graphene} = \frac{\epsilon_0 \epsilon_r}{d_{Al2O3}} \frac{A_{tip}}{A_{graphene}} = 26.6 \ \text{(nF/cm}^{-2}\text{)} \tag{S2}$$

During our experiment, the tip was contact with the center of the graphene ribbon and the indenter tip was grounded. So, the voltage between the graphene and the indenter tip was about half of the bias voltage. In our measurement, the bias voltage is 10 mV, so the gate effect from the tip is corresponding to 35 mV back gating from the Si substrate. Comparing to the gate voltage we added, this voltage is negligible.

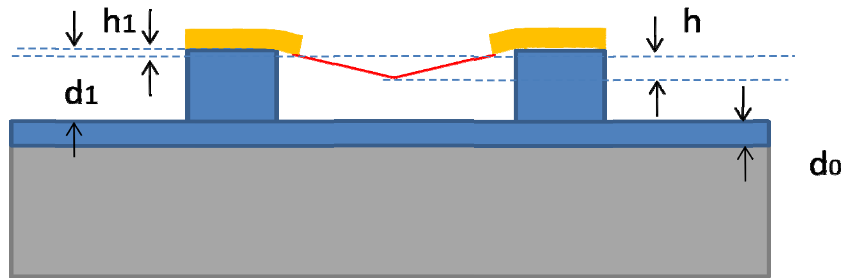

Figure S3, Illustration of indenting a suspended graphene device.

Now, we turn to calculate the gate capacitance change during the indentation process. The indenter tip pushes the graphene toward the Si substrate, thereby increasing the gate capacitance, as shown schematically in Fig. s3. The capacitance between SiO_2 and graphene can be expressed as:

$$C_{graphene-SiO2} = 2\epsilon_0 \int_0^{l/2} \frac{w dx}{2hx/l + d_1 - h - h_1} = \frac{\epsilon_0 w l}{h} Ln\left(\frac{d_1 - h_1}{d_1 - h_1 - h}\right) \tag{S3}$$

where h and h_1 is the deflection of the center of the graphene ribbon and the bending deflection of the electrodes. The gate capacitance can then be derived as:

$$C_{back}/A_{graphene} = \frac{\epsilon_0 \epsilon_r}{d_0 + \epsilon_r h / Ln(\frac{d_1 - h_1}{d_1 - h_1 - h})} \quad \text{(S4)}$$

Based on this equation, the relative change of gate capacitance can be calculated and is plotted in the inset of Fig. 3C. As we can see, the calculated values match the results extracted from experimental data very well.

MD simulation details

We constructed a 25 x 37 nm graphene nanoribbon (Fig. S4) by replicating the orthorhombic graphene crystal structure (a0 = 4.275Å, b0 = 4.93670Å). We then subjected the replicated cell to 500 steps of conjugate gradient minimization, with a force tolerance of 10E-4. We equilibrated the structure at room temperature for 1ns of molecular dynamics in the canonical (NVT) ensemble. The temperature of the nanoribbon was controlled with a Nose-Hoover thermostat and a temperature coupling constant of 100fs. The cell was then indented the center of the nanoribbon with a cylindrically repulsive ($1/r^9$) potential along z dimension in the isobaric (NPT) ensemble with a piston coupling constant of 2.0ps. The Nose-Hoover barostat was only applied along the y-direction, allowing the cell to shrink in response to the applied stress. The system was indented to a maximum depth of 10nm (14% strain) over 10 ns (a tip velocity of 1 m/s). All simulations were performed with the LAMMPS[4] 2001 atomistic simulator.

Obtaining the relative resistivity from DFT

All DFT calculations are performed using generalized gradient approximation by Perdew-Burke-Ernzerhof (PBE)[5] with the projector-augmented wave (PAW) method[6, 7] as implemented in VASP[8]. The simulation cell is orthorhombic cell containing 4 carbon atoms; x-axis is chosen as an armchair direction and y-axis is chosen as a zigzag direction. The cut-off value of the plane-wave basis set is given by 500 eV and 24×24 k-points are sampled from reciprocal space using Monkhorst-Pack method. We first obtained a stress-free state by optimizing the atomic positions and cell parameters, then, deformed the simulation cell by 1) stretching the armchair direction up to 2% and 2) compressing the zigzag direction up to 0.333%, simultaneously. This leads us to maintain the Poison ration value as 0.17. Local band structure near the Dirac point is obtained from each simulation set. Then, we linearly fitted the band structure to obtain the Fermi velocity.

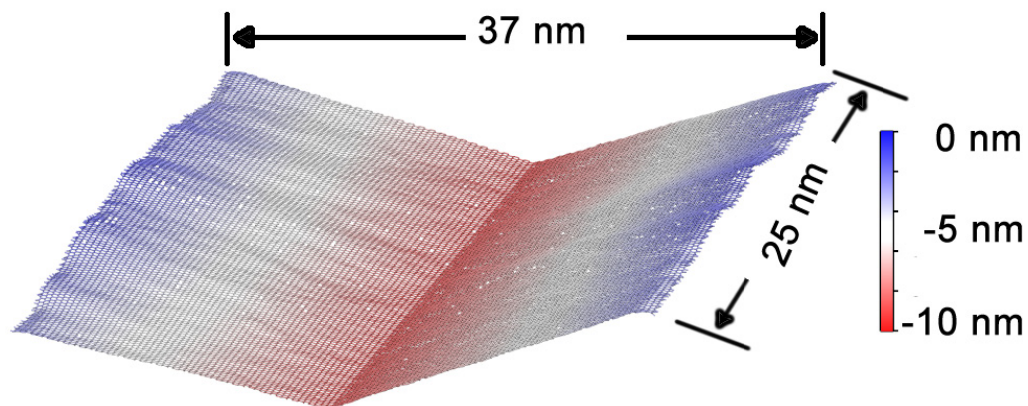

Figure S4: Schematic of MD simulation unit cell. The nanoribbon is periodic in the y direction and finite in the x direction. The effect of the electrode is simulated by fixing two layers of carbon atoms at the boundary. The center of the nanoribbon is subjected to a cylindrically symmetric repulsive along the z-axis and indented to a depth of 10nm (about 14% strain).

References

1. Novoselov, K. S.; Geim, A. K.; Morozov, S. V.; Jiang, D.; Zhang, Y.; Dubonos, S. V.; Grigorieva, I. V.; Firsov, A. A. *Science* 2004, 306, (5296), 666-669.
2. Ferrari, A. C.; Meyer, J. C.; Scardaci, V.; Casiraghi, C.; Lazzeri, M.; Mauri, F.; Piscanec, S.; Jiang, D.; Novoselov, K. S.; Roth, S.; Geim, A. K. *Physical Review Letters* 2006, 97, (18), 187401.
3. Stolyarova, E.; Stolyarov, D.; Bolotin, K.; Ryu, S.; Liu, L.; Rim, K. T.; Klima, M.; Hybertsen, M.; Pogorelsky, I.; Pavlishin, I.; Kusche, K.; Hone, J.; Kim, P.; Stormer, H. L.; Yakimenko, V.; Flynn, G. *Nano Letters* 2009, 9, (1), 332-337.
4. Plimpton, S. *Journal of Computational Physics* 1995, 117, (1), 1-19.
5. Perdew, J. P.; Burke, K.; Ernzerhof, M. *Physical Review Letters* 1996, 77, (18), 3865-3868.
6. Blochl, P. E.; Jepsen, O.; Andersen, O. K. *Physical Review B* 1994, 49, (23), 16223-16233.
7. Kresse, G.; Joubert, D. *Physical Review B* 1999, 59, (3), 1758-1775.
8. Kresse, G.; Furthmuller, J. *Computational Materials Science* 1996, 6, (1), 15-50.